Structural morphology and Mn distribution in annealed InP coimplanted with P and Mn

I. G. Bucsa,[a] R. W. Cochrane, and S. Roorda
Regroupement québécois sur les matériaux de pointe and Département de physique, Université de Montréal, C.P. 6128, succursale Centre-Ville, Montréal, Québec H3C 3J7, Canada

(Received 4 August 2009; accepted 9 February 2010; published online 12 April 2010)

We have studied the structural, chemical, and magnetic properties of InP following coimplantation with high energy P and Mn ions to fluences in excess of 10^{16} cm^{-2} and subsequent annealing above 600 °C. Rutherford backscattering spectrometry, x-ray diffraction, secondary ion mass spectrometer, and transmission electron microscopy measurements reveal that rapid thermal annealing causes only a partial epitaxial recrystallization of the layer amorphized by the implantations; the remaining region up to the surface crystallizes incoherently but retains most of the implanted Mn. Magnetic measurements demonstrate that fully three quarters of the Mn has been incorporated into MnP nanoparticles embedded into this polycrystalline InP region. The remaining Mn is most probably incorporated into the InP lattice but gives only a paramagnetic response that can be described by a simple Brillouin function at temperatures down to 5 K. © *2010 American Institute of Physics*. [doi:10.1063/1.3357381]

I. INTRODUCTION

Ferromagnetic semiconductor structures have been proposed[1] for possible applications in new electronic devices that make use of both the spin and the charge of the electron. However, producing such ferromagnetic structures with transition temperatures above 300 K has proven elusive. Attempts to introduce a few percent of Mn into III-V hosts by molecular beam epitaxy (MBE) and metal organic chemical vapor deposition (MOCVD) of GaAs:Mn and GaP:Mn (Refs. 2–5) often result in the formation of MnAs or MnP magnetic particles embedded in the semiconducting host. Since Mn has very low solubility in the semiconducting material,[6] annealing of Mn-implanted GaAs, GaP, or InP at temperatures above 600 °C (Refs. 7 and 8) gives sufficient energy to the Mn atoms to diffuse and form such magnetic compounds.

In recent work[8] we have studied InP and GaP substrates implanted with 200 keV Mn ions to a fluence of 3×10^{16} cm^{-2} and subsequently given a rapid thermal anneal (RTA). Rutherford backscattering spectrometry (RBS) and x-ray diffraction (XRD) measurements demonstrated that implantation gives rise to an amorphous layer about 320 nm thick at the surface. Upon annealing above 600 °C, this damaged layer regrows epitaxially on the substrate via the passage of a recrystallization front from the interior toward the surface. This front also drives most of the Mn atoms into a narrow surface layer where a significant fraction of them form magnetic MnP nanoparticles. At the annealing temperatures used it is clearly energetically more favorable for Mn to form MnP crystals, rather than metallic Mn or other chemical compounds. Similar segregation has been observed in high fluence (10^{16} cm^{-2}) Mn-implanted GaAs substrates where MnAs particles form at the surface.[6]

For practical applications it is desirable to control the distribution of the magnetic particles within the semiconductor host. Reduction in the outward diffusion of the *p*-type impurities has been successfully demonstrated in InP (Refs. 9 and 10) by coimplantation of *p*-type impurities (Zn and Be) and various group V elements. It was suggested that supplementary quantities of group V elements in InP create In vacancies that trap *p*-type impurities, as it is known that these impurities usually substitute for In. Substitutional impurities created in this way are much less mobile than interstitial ones, resulting in a significant reduction in the outward diffusion during subsequent annealing. Since Mn is a *p*-type impurity, and substitutes for In when introduced into InP,[11] these studies suggest that coimplantation of Mn and P could be effective in inhibiting Mn segregation to the surface during annealing.

In this paper, we report the influence of coimplantation of P and Mn in InP on the spatial distribution of Mn atoms and the formation of MnP particles after annealing at temperatures above 600 °C, since lower annealing temperatures do not produce epitaxial regrowth of the damaged implantation layer. We show that this procedure strongly reduces the Mn outward diffusion and surface segregation when compared to Mn-implanted samples. As the quantity of Mn introduced into InP (up to 5 at. %) is well beyond the solubility limit, MnP particles are formed during annealing, but remain distributed throughout the implanted layer with only a small segregation to the surface. Magnetic measurements also reveal that about a quarter of the implanted Mn is found to be in a paramagnetic state at liquid He temperatures. If this paramagnetic Mn is indeed incorporated substitutionally into the InP matrix, these measurements fix an upper bound on the ferromagnetic transition temperature of such a dilute magnetic semiconductor.

II. EXPERIMENTAL DETAILS

InP(001) substrates, Fe-doped (semi-insulating, $p \sim 10^{16}$ cm^{-3}), were implanted with P at fluences up to 3

[a]Electronic mail: ig.bucsa@umontreal.ca.

TABLE I. List of the implantation fluences and energies for the principal samples reported in this paper.

Sample	P fluence (ions/cm^2)	P energy (keV)	Mn fluence (ions/cm^2)	Mn energy (keV)
A	3×10^{16}	120	3×10^{16}	200
B	2×10^{16}	300 @ 45°	3×10^{16}	200
C	1.5×10^{16}	120	3×10^{16}	200
D	0	0	3×10^{16}	200

$\times10^{16}$ cm^{-2}, and with Mn ions at a fluence of 3×10^{16} cm^{-2} using the 1.7 MV tandetron accelerator on the Université de Montréal campus. The ion energies and fluences for the principal samples reported in this paper are listed in Table I:

Implantations were carried out at normal incidence except for sample B. Monte Carlo simulations with the TRIM (Ref. 12) code give that Mn at 200 keV and P at 120 keV at normal incidence both have a range of 130 nm and a maximum penetration depth of 320 nm. Sample B was implanted with P at an energy of 300 keV at an angle of incidence of 45° for which the ion range is 215 nm with a maximum penetration depth of 460 nm. Most of the measurements reported herein were obtained on samples A and B.

After implantation and initial characterization, samples were subjected to a RTA at temperatures between 600 and 650 °C for 30–120 s under a nitrogen flow using samples mounted face-to-face with a piece of the substrate material to protect against phosphorus loss. The crystal structure of the samples was probed with a Philips X'pert x-ray powder diffractometer in the theta-2-theta configuration, using a Cu K_α beam ($\lambda=0.154$ nm) that also contain about 1% of K_β radiation ($\lambda=0.139$ nm). RBS was carried out with a 2 MeV He beam generated by the tandetron accelerator using a detector situated at an angle of 10 degrees with respect to the incident beam. For the RBS analysis, samples were mounted on a computer-controlled three-axis goniometer in order to perform measurements along both channelling—InP(001)—and random directions.

Atomic concentration profiles were measured with a time-of-flight secondary ion mass spectrometer (IONTOF model TOF.SIMS IV) before and after annealing. In order to calibrate the depth scale, the depth of the sputtered crater at the end of the SIMS analysis was measured with a Dek-Tak profilometer. Subsequently, the measured Mn profile was normalized by equating the integrated concentration to the implanted fluence.

Cross sectional transmission electron microscopy (TEM) analyses were performed on a JEOL 2100F microscope equipped with a field-emission electron source operated at 200 kV. This instrument is also equipped with an x-ray detector capable of energy dispersive x-ray spectrometry (EDS) mapping of the samples with the microscope in the scanning mode. Bright field, dark field, and also scanning transmission electron microscopy (STEM) images were taken.

Magnetic moment data were measured with a superconducting quantum interference device (SQUID) from Quantum Design, and a vibrating sample magnetometer (VSM) from ADE Technologies. Most of the data were obtained with the applied magnetic field oriented along the [110] axis of InP (in the plane of the sample).

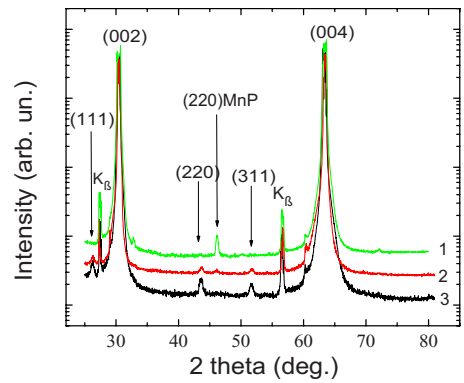

FIG. 1. (Color online) θ-2θ XRD spectra for three InP(Fe) samples implanted and RTA annealed at 650 °C for 1 min: (1) sample D; (2) sample C; and (3) sample A.

III. EXPERIMENTAL RESULTS

A. XRD

θ-2θ scans on [001] oriented InP substrate show only the (002) and (004) peaks of the InP lattice for 2θ angles smaller than 90 degrees. After implantation of either Mn or P and Mn, these peaks are substantially broadened, and show a substructure consistent with a slight curvature of the sample (radius of curvature of order 0.5 m). In addition, a large background at low angles appears, arising from the formation of an amorphous layer at the surface. Subsequent RTA treatment above 600 °C results in the disappearance of the low-angle background in the x-ray spectra, but does not significantly change the sample curvature.

Figure 1 shows XRD spectra for three implanted samples (A, C, and D) after RTA treatment at 650 °C for 60 s. Several weak peaks can be seen in addition to the (002) and (004) peaks of the substrate. In the Mn-only implanted sample D (spectrum 1 of Fig. 1), a small peak appears that can be identified as the (220) reflection of orthorhombic MnP. This peak is present only in samples displaying the magnetic signature of MnP. Since this particular diffraction peak is not the most intense for MnP, one concludes that there is a tendency for some of the MnP particles to form with a texture in which the (220) planes are parallel to (002) planes of the substrate. For this orientation, the magnetically easy c-axis of MnP lies in the plane of the sample. A similar texture has been found in the MOCVD-grown samples discussed in Ref. 8.

Spectrum 2 indicates that for sample C with a P fluence of 1.5×10^{16}, the (220) MnP peak (i.e., the MnP texturing) has been reduced but a slight polycrystallinity has been introduced into the InP matrix. For sample A (spectrum 3) with twice the P fluence, the MnP texturing has disappeared and the InP polycrystallinity has increased. As will become clear with the structural measurements to follow, the disappearance of the MnP texturing and the appearance of the polycrystallinity are closely interconnected.

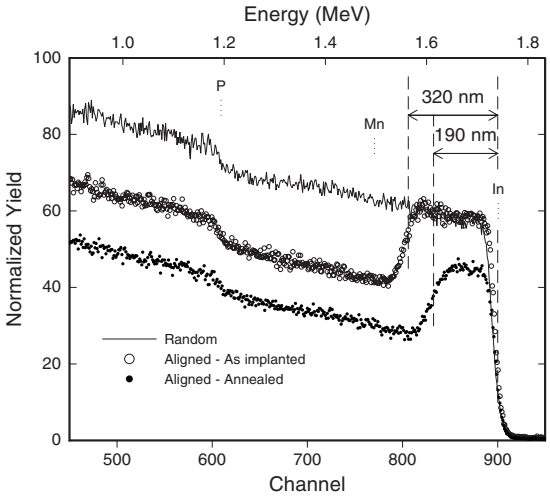

FIG. 2. RBS channelled spectrum (squares) for sample A. For comparison, the random spectrum (line) and the channelled spectrum for an unannealed Mn-implanted sample are also plotted. The surface positions of In, Mn, and P are indicated on the figure.

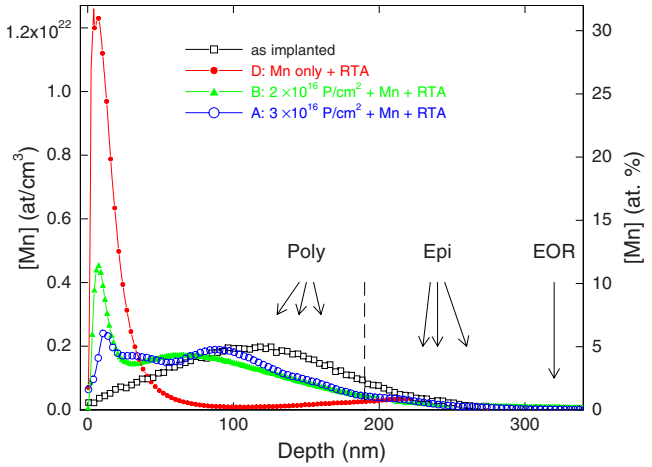

FIG. 3. (Color online) Mn concentration profiles in InP(Fe) measured by SIMS for four samples as indicated. The annealing was done at 650 C for 1 min for three of the samples.

B. Rutherford backscattering

RBS measurements for annealed sample A coimplanted with P and Mn to the same depth are presented in Fig. 2. The spectrum of the as-implanted sample in the channelling direction corresponds to an amorphous layer 320 nm thick at the surface of the InP substrate.[8] After annealing, there is partial reparation of the damage which results in a shrinking of the disordered layer at the surface to a thickness of 190 nm. Comparing the RBS channelled and random spectra leads to the conclusion that 130 nm of the initially amorphized layer next to the substrate have epitaxially regrown during the RTA treatment. Drawing on the XRD results of Sec. III A, the disorder observed in the 190 nm layer at the surface arises because this layer is polycrystalline and not orientationally coherent with the substrate. Furthermore, since the random and channelled spectra are not at the same height at the high energy end of the spectrum, some channelling is occurring through this 190 nm layer indicating that, although polycrystalline, it does not have a completely random structure.

C. SIMS

In Fig. 3 are plotted Mn SIMS profiles in a Mn-implanted sample (D) before and after annealing, as well as in two samples (A and B) coimplanted with P and Mn and annealed. The concentration for the unannealed sample has a Gaussian-like profile that is in good agreement with Monte Carlo simulations done with the TRIM code. A similar Mn profile was also obtained for an unannealed sample coimplanted with P and Mn.

The profile for the Mn-only implanted sample D reveals that, during the annealing, most of the Mn segregates to the surface. (This profile was also presented in our previous publication, Ref. 8.) In the coimplanted samples A and B, the situation is very different: one still observes some Mn diffusion to the surface, but to a significantly smaller extent than for sample D. For sample A with the highest P fluence, the Mn displacement toward the surface is the least of the three coimplanted materials. For samples B and C (the profile for C is not shown but is very similar to that of B) with smaller P fluences the Mn has been pushed closer to the surface. It should be noted that for sample B the P was implanted beyond the Mn, while for A and C the Mn and P distributions overlapped. Finally, all the SIMS profiles for the annealed material have identical Mn concentration profiles throughout the epitaxially regrown layer beyond 200 nm from the surface.

D. TEM

TEM measurements of sample A coimplanted with equal fluences of Mn and P to the same depth and annealed at 650 °C are presented in Figs. 4 and 5. Figure 4(a) is a bright field image of the entire implanted layer from the surface to beyond the ion range of 320 nm. Two distinct regions are visible throughout the implanted zone: the top 190 nm appears as a bright, relatively homogeneous zone while the region from this point to the end of the implanted zone shows up as a dark band. Based on the results of Secs. III A–III C, this latter zone is epitaxially coherent with the substrate beyond; the dark band arises from the presence of dislocations and other defects generated during the recrystallization process. Figure 4(b) presents a high-resolution image at the interface between the dark and bright bands in Fig. 4(a) where crystalline InP planes with different orientations can be discerned, indicating that, at this depth (190 nm), the implanted layer is no longer completely coherent with the substrate. At 100 nm from the surface, in the polycrystalline layer, MnP crystals with dimensions between 5 and 10 nm can be identified in the high-resolution image shown in Fig. 4(c). The lattice distances given in the figure correspond to the (111) (3.93 Å) and (110) planes (2.47 Å) of MnP. InP grains with mean sizes of 5 nm can also be observed by high-resolution imaging (not shown here) in this polycrystalline layer.

Chemical analysis of sample A was obtained by EDS mapping in the region selected in Fig. 5(a). The Mn map [Fig. 5(b)] indicates the formation of Mn clusters, of 70 nm

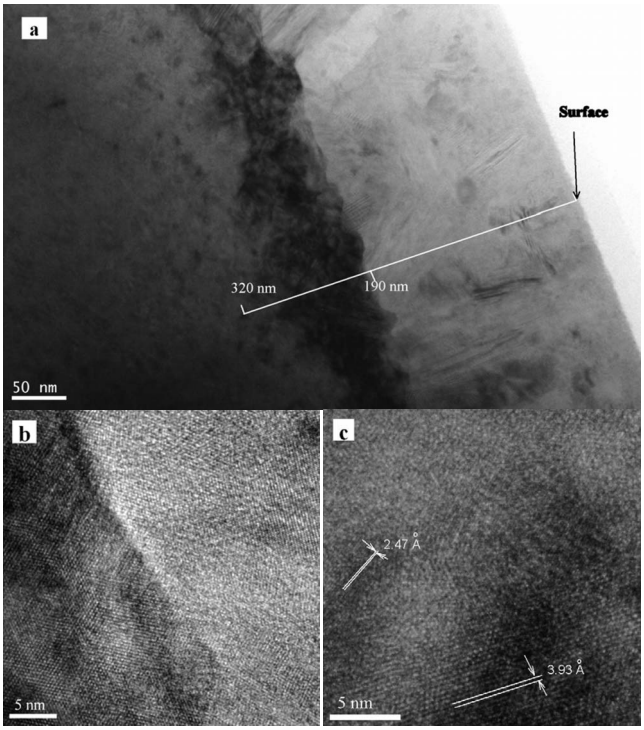

FIG. 4. (a) Bright field TEM image of sample A; high-resolution TEM images taken (b) at the interface between the dark and bright regions in (a) and (c) at 100 nm from the surface.

mean size, distributed throughout the entire implanted layer and not only at the surface as was the case for samples implanted only with Mn.[7,8] This map shows two maxima of the Mn concentration, approximately 70–80 nm apart, in good agreement with the SIMS concentration profile of Fig. 3.

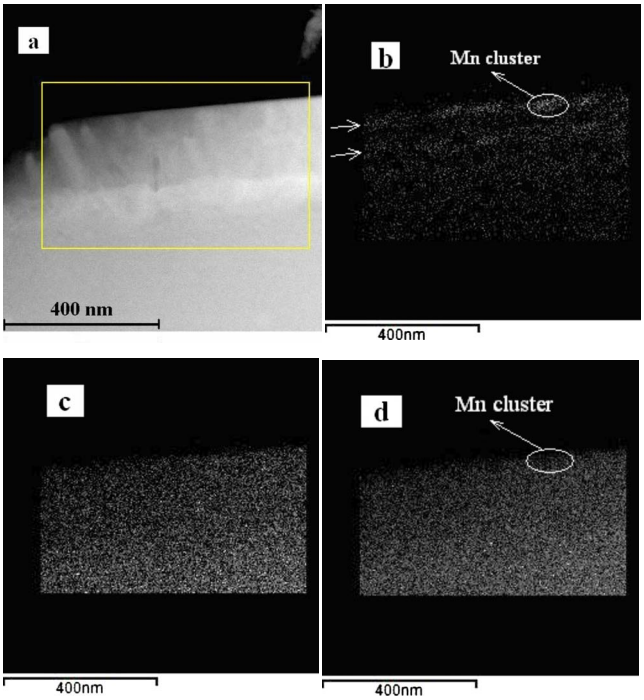

FIG. 5. (Color online) (a) an STEM image of sample A; the yellow rectangle represents the area where the EDS mapping was carried out; (b), (c), and (d) are the EDS maps of Mn, P, and In, respectively. The arrows in figure (b) indicate the positions with the maximum Mn concentration.

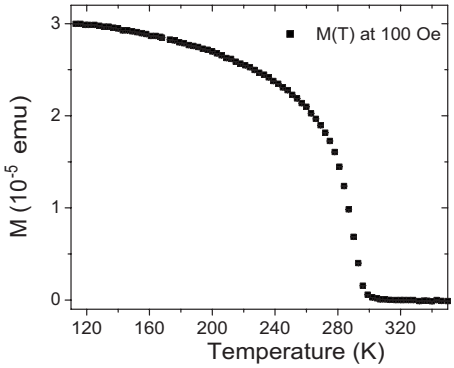

FIG. 6. The field-cooled magnetization of sample B at 100 Oe.

This agreement provides confidence that the SIMS concentration profiles are not influenced by matrix effects due to the variation in the Mn concentration with depth. However, neither the EDS maps nor the SIMS profiles supplies information on the chemical bonding of the Mn, either in the form of MnP particles or of Mn otherwise dispersed throughout the InP matrix. Finally, the EDS mappings also reveal constant concentrations of P and In across the material [Figs. 5(c) and 5(d)] and thus a good stoichiometry on scales greater than 10 nm. The only exception occurs near the surface where the regions rich in Mn are depleted in In.

E. Magnetic measurements

Magnetic measurements on unannealed samples show only a diamagnetic signal at temperatures above 100 K and no indication of ferromagnetism. After annealing above 600 °C clear evidence of ferromagnetism is observed for all samples. Figure 6 presents the temperature dependence of the magnetic moment of sample B cooled in an applied field of 100 Oe. The figure gives definitive evidence for a ferromagnetic transition with a Curie temperature of $T_c = 290 \pm 3$ K, a clear signature of MnP.[13] The field and temperature behavior of the ferromagnetic material is quite complicated: field-cooled and zero-field-cooled magnetizations deviate below 280 K and magnetization curves below this temperature show significant hysteresis with coercivities greater than 2 kOe below 200 K. Similar behavior has been reported for samples implanted only with Mn.[8]

Recently we have been able to extend the magnetic measurements to lower temperatures and higher applied fields. In Fig. 7, we present magnetization curves for sample B at 110 and 5 K. These measurements demonstrate that the high coercivity persists to liquid helium temperatures and that complete saturation requires fields of at least 30 kOe. In both Figs. 6 and 7, the measurements were made with the field applied in the sample plane parallel to the [110] direction of the InP substrate. As was also noted in Ref. 8 for samples implanted only with Mn, the coercivity and also the remanence below T_c is anisotropic, varying approximately 25% for fields applied perpendicular to the [110] direction.

Further examination of Fig. 7 shows a surprisingly large increase in the magnetic moment at the highest fields (nearly 50%) on cooling from 110 to 5 K. However, direct measurements on a MnP single crystal[13] give only a 5% change in the

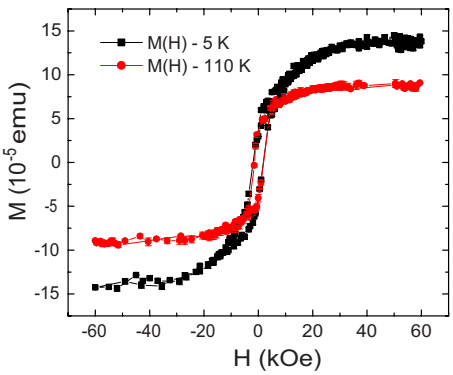

FIG. 7. (Color online) Magnetic moment curves for sample B at 5 and 110 K measured in-plane in the [110] direction.

saturation magnetization between these temperatures. We conclude that there is a second contribution to the sample moment, other than that of the MnP particles, that gives rise to the additional moment as the temperature is lowered below 100 K. The field dependence of this additional component suggests that the Mn is in a paramagnetic state that can be described by Brillouin function. In order to clarify and quantify this possibility, the magnetization was measured as a function of temperature in an applied field of 10 kOe. The results are given in Fig. 8. Below 50 K there appears a clear T^{-1} variation of the magnetic moment demonstrating Curie or Curie Weiss behavior, as would be expected for a contribution to the moment with a Brillouin function field dependence at 5 K.

IV. DISCUSSION

The data presented in the previous section can be interpreted within the framework of a model of the structural evolution of the implanted material upon annealing at temperatures above 600 °C.

A. Structural morphology

As detailed in reference,[8] implantation of energetic Mn ions at fluences above 10^{16} cm^{-2} causes an amorphization of

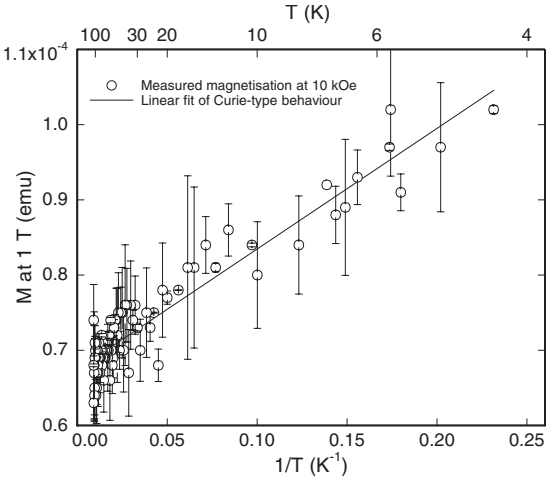

FIG. 8. Magnetic moment of sample B at an applied field of 10 kOe as a function of the inverse temperature.

the substrate to depths exceeding 300 nm. Annealing above 600 °C generates a growth front that recrystallizes the amorphous layer epitaxially, displacing most of the implanted Mn up to the surface in the process. This outward displacement occurs in spite of the fact that the normal diffusion process would be driving some of the Mn toward the interior of the sample.

For samples coimplanted with energetic P as well as Mn, epitaxial regrowth is also initiated during annealing above 600 °C, but is stalled well before reaching the surface; the remaining layer recrystallizes incoherently resulting in a polycrystalline surface layer about 200 nm thick. During this process much of the Mn is expelled from the epitaxially layer, but a large fraction of it is retained within the polycrystalline surface layer. Thus, coimplantation of P has resulted in a different morphology for the annealed material as well as an increase in the amount of Mn trapped within the interior of the layer. This trapping of the Mn cannot be simply due to the increased damage produced in samples coimplanted with P, since it has been shown[8] that the initial Mn implantation had already rendered the surface layer amorphous to a depth of 320 nm. Moreover, the Mn profile shows neither discontinuity nor maximum at the interface between the crystalline and polycrystalline regions.

The central question is how the presence of excess P can change the morphology in the described way. To answer this question we propose the following scenario based on the mechanism mentioned in the Introduction that coimplanted P results in an increase in the concentration of In vacancies during the epitaxial growth stage. These In vacancies can trap Mn atoms, effectively increasing the Mn solubility. This Mn incorporation results in a slightly different lattice parameter which gives rise to elastic strain within the growing matrix. The strain in turn generates dislocations and other defects that cause the epitaxial recrystallization to break down. Quantitatively the Mn concentration of the coimplanted material at the epitaxial-polycrystalline interface as measured by SIMS is approximately 1 at. %. If this concentration of Mn were substitutionally incorporated into the InP matrix, a calculation, taking into account the ion radii of Mn and In, leads to a diminished lattice parameter for InP of 0.6%. Such a strain is certainly high enough to produce dislocations, as required by the present model. Within this model, 1 at. % would therefore be the maximum concentration of Mn that InP can maintain during rapid epitaxial regrowth of the amorphous layer during annealing.

Closer to the surface where the Mn concentration is the highest, MnP particles nucleate inside the polycrystalline region. In the Mn-only implant case, all the Mn is swept to the free surface where it forms MnP nanoparticles. In the case of Mn and P coimplantation, after the epitaxy breaks down, crystallization proceeds in random directions and grain boundaries form which could provide nucleation sites for MnP particles buried within the polycrystalline layer, as observed.

In support of the model, TEM images show a much higher density of dislocations throughout the epitaxial layer compared to the polycrystalline layer. In addition, SIMS measurements reveal that the interface between these layers

occurs at the point where the Mn concentration of the coimplanted material begins to rise significantly above that of the Mn-only implanted sample. Unfortunately, XRD measurements are unable to detect this strain because the signal from the very thin strained layer is lost within that of the substrate which has been broadened by the induced curvature of the sample.

B. Distribution of the implanted Mn

The presence of MnP particles is observed directly in the TEM data, but it is the magnetic data that confirm that most of the available Mn has been incorporated into these particles. All annealed samples whether coimplanted with P or not exhibit the magnetic signature of MnP.

One very useful advantage of implanting the Mn is that it permits a quantitative accounting of its subsequent distribution. Using the data of Fig. 7, the saturation magnetic moment at 110 K for the MnP component of the signal is found to be $8.5 \pm 0.5 \times 10^{-5}$ emu. Since the reported magnetic moment of MnP is 1.29 Bohr magnetons/Mn-atom,[13] the number of Mn atoms incorporated into the MnP phase is calculated to be $7.2 \pm 0.4 \times 10^{15}$. Furthermore, assuming that the paramagnetic contribution shown in Fig. 8 arises from free, noninteracting Mn spins ($g=2$, $J=5/2$) not incorporated into the MnP particles, one obtains $N=2.0 \pm 0.1 \times 10^{15}$, for a total estimate of $9.2 \pm 0.5 \times 10^{15}$ Mn atoms for this sample. Given the surface area of the sample, the total number of Mn atoms implanted is $8.5 \pm 0.9 \times 10^{15}$. Within experimental uncertainties, all of the implanted Mn has been accounted for. As a confirmation, adding to the 110 K data of Fig. 7 the appropriate Brillouin function for the number of paramagnetic Mn calculated reproduces precisely the 5 K data.

For this sample (B), the presence of excess P has resulted in the incorporation of 78% of the available Mn into MnP particles. This fraction is substantially higher than that for the Mn-only implanted material (31%) (Ref. 8). The remaining 22% of the Mn is dispersed throughout the matrix as isolated paramagnetic impurities. It is tempting at this point to speculate that the paramagnetic part represents the Mn incorporated into the epitaxially regrown layer and that the MnP particles are imbedded in the polycrystalline layer. In any case, the measurements fix an upper bound of several Kelvins on any possible ferromagnetic transition temperature for the Mn not incorporated into the MnP particles. Indeed, given that the nonuniform distribution of the Mn, even this estimate of a possible ferromagnetic transition temperature is overly optimistic.

Dilute magnetic semiconductors with critical temperatures up to 200 K have been reported for Mn thermally diffused into InP (Ref. 14) and MBE-grown GaMnAs (Ref. 15) produced at temperatures below 300 °C. For Mn-implanted and annealed InP there are reports of the formation of MnP, as well as of a diluted magnetic semiconductor with T_c near 90 K (Ref. 16) and also of the formation of the $InMn_3$ magnetic phases.[17] However, for the materials reported in the present paper most of the Mn is incorporated into ferromagnetic MnP nanoparticles while the remainder gives a paramagnetic response at all temperatures down to 5 K. Any second ferromagnetic phase transition would only occur at much lower temperatures.

V. CONCLUSION

In summary, we have demonstrated that coimplantation of P and Mn into InP followed by high temperature annealing is an effective method for the formation of MnP particles within the surface layer of the host matrix, but at a cost of the structural coherence of the layer. A consequence of P coimplantation (instead of simple Mn implantation) is that a small fraction of the Mn is incorporated into the InP matrix to a local concentration not exceeding 1%. Magnetically, this latter part displays a simple paramagnetic behavior down to 5 K. Within the field of magnetic semiconductor structures, it seems clear that the present approach using ion implantation followed by high temperature annealing will not result in InP-based dilute magnetic semiconductors of practical utility. The high annealing temperatures required to repair the structural damage from the implantation process promote the precipitation of MnP even though coimplantation of P helps to achieve some integration of the Mn into the InP matrix.

ACKNOWLEDGMENTS

We acknowledge helpful discussions with David Ménard, Patrick Desjardins, and Remo Masut about their MOCVD-grown GaMnP samples. In addition, we thank Martin Chicoine, Louis Godbout, and Louis-Philippe Carignan for their assistance with the ion implantation and the VSM measurements, as well as Patrick Fournier for access to his SQUID magnetometer and Mangala Singh for help with the measurements. This research has been supported by NSERC, Canada and FQRNT, Québec.

[1] F. Matsukura, H. Ohno, A. Shen, and Y. Sugawara, Phys. Rev. B **57**, R2037 (1998).
[2] M. Moreno, A. Trampert, B. Jenichen, L. Daveritz, and H. K. Ploog, J. Appl. Phys. **92**, 4672 (2002).
[3] J. De Boeck, R. Oesterholt, A. Van Esch, H. Bender, C. Bruynseraede, C. Van Hoof, and G. Borgs, Appl. Phys Lett. **68**, 2744 (1996).
[4] M. Yokohama, H. Yamaguchi, T. Ogawa, and M. Tanaka, J. Appl. Phys. **97**, 10D317 (2005).
[5] S. Lambert-Milot, C. Lacroix, D. Ménard, R. A. Masut, P. Desjardins, M. Garcia-Hernandez, and A. de Andres, J. Appl. Phys. **104**, 083501 (2008).
[6] R. Moriya and H. Munekata, J. Appl. Phys. **93**, 4603 (2003).
[7] O. D. D. Couto, Jr., M. J. S. P. Brasil, F. Yikawa, C. Giles, C. Adriano, J. R. R. Bortoleto, M. A. A. Pudenzi, H. R. Gutierrez, and I. Danilov, Appl. Phys. Lett. **86**, 071906 (2005).
[8] I. G. Bucsa, R. W. Cochrane, and S. Roorda, J. Appl. Phys. **106**, 013914 (2009).
[9] K. M. Yu and M. C. Ridgway, Nucl. Instrum. Methods Phys. Res. B **168**, 65 (2000).
[10] M. V. Rao and R. K. Nadella, J. Appl. Phys. **67**, 4 (1990).
[11] S. Adachi, *et al.*, *Properties of Indium Phosphide* (INSPEC, The Institution of Electrical Engineers, London and New York, 1991).
[12] J. F. Ziegler, J. P. Biersack, and U. Littmark, *The Stopping and Range of Ions in Solids* (Pergamon, New York, 1985).
[13] E. E. Huber and D. H. Ridgley, Phys. Rev. **135**, A1033 (1964).
[14] Y. Shon, H. C. Jeon, S. Lee, S.-W. Lee, D. Y. Kim, T. W. Kang, E. K. Kim, C. S. Yoon, C. K. Kim, Y. J. Park, Y. Kim, J. M. Baik, and J. L. Lee, J. Cryst. Growth **297**, 289 (2006).

[15]K. Ohno, S. Ohya, and M. Tanaka, J. Supercond. Novel Magn. **20**, 417 (2007).
[16]Y. Shon, W. C. Lee, Y. S. Park, Y. H. Kwon, S. J. Lee, K. J. Chung, H. S. Kim, D. Y. Kim, D. J. Fu, T. W. Kang, X. J. Fan, Y. J. Park, and H. T. Oh, Appl. Phys. Lett. **84**, 2310 (2004).
[17]Y. Shon, S. Lee, H. C. Jeon, S. W. Lee, D. Y. Kim, T. W. Kang, E. K. Kim, D. J. Fu, X. J. Fan, C. S. Yoon, and C. K. Kim, Appl. Phys. Lett. **88**, 232511 (2006).